Broadband High-Efficiency Half-Wave Plate: A Supercell-Based Plasmonic Metasurface Approach

Fei Ding,[†,‡,⊥] Zhuoxian Wang,[†,⊥] Sailing He,[*,‡,§] Vladimir M. Shalaev,[†] and Alexander V. Kildishev[*,†]

[†]Birck Nanotechnology Center, School of Electrical & Computer Engineering, Purdue University, West Lafayette, Indiana 47907, United States, [‡]State Key Laboratory of Modern Optical Instrumentations, Centre for Optical and Electromagnetic Research, Zhejiang University, Hangzhou 310058, China, and [§]Department of Electromagnetic Engineering, School of Electrical Engineering, Royal Institute of Technology, S-100 44 Stockholm, Sweden. [⊥]F. Ding and Z. Wang contributed equally to this work.

ABSTRACT

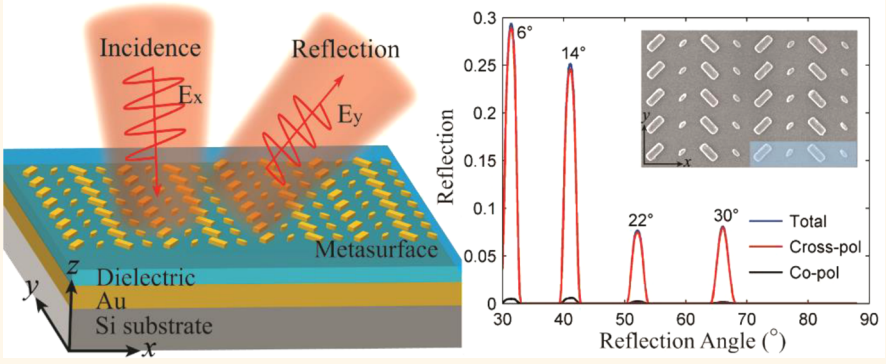

We design, fabricate, and experimentally demonstrate an ultrathin, broadband half-wave plate in the near-infrared range using a plasmonic metasurface. The simulated results show that the linear polarization conversion efficiency is over 97% with over 90% reflectance across an 800 nm bandwidth. Moreover, simulated and experimental results indicate that such broadband and high-efficiency performance is also sustained over a wide range of incident angles. To further obtain a background-free half-wave plate, we arrange such a plate as a periodic array of integrated supercells made of several plasmonic antennas with high linear polarization conversion efficiency, consequently achieving a reflection-phase gradient for the cross-polarized beam. In this design, the anomalous (cross-polarized) and the normal (copolarized) reflected beams become spatially separated, hence enabling highly efficient and robust, background-free polarization conversion along with broadband operation. Our results provide strategies for creating compact, integrated, and high-performance plasmonic circuits and devices.

KEYWORDS: metasurface · half-wave plate · plasmonic antennas · background-free

Polarization is an important characteristic of light. The capability of controlling and manipulating the polarization states of light is of vital importance in a variety of consumer products, science, and high-tech applications. Conventional methods to modulate polarizations utilize birefringence in crystals, which causes phase retardation between the two orthogonally polarized wave components. In this way, the polarization change is gradually accumulated during light propagation; thus the resulting optical components usually suffer from specific thickness limitations and bulky configurations, which goes against the general trend of integration and miniaturization in photonics.

Recently, metasurfaces—the two-dimensional (2D) version of metamaterials—have been gaining increasing attention due to their remarkable abilities in light manipulation, versatility, ease of on-chip fabrication, and integration owing to their planar profiles.[1,2] Many exotic phenomena and useful flat optical devices have been demonstrated, such as anomalous reflection/refraction,[3−7] surface wave coupling,[8−10] planar focusing lenses,[11−13] and high-resolution optical holograms.[14−16] In general, metasurfaces can release our dependence on the

* Address correspondence to kildishev@purdue.edu, sailing@zju.edu.cn.

Received for review January 12, 2015 and accepted March 19, 2015.

Published online 10.1021/acsnano.5b00218

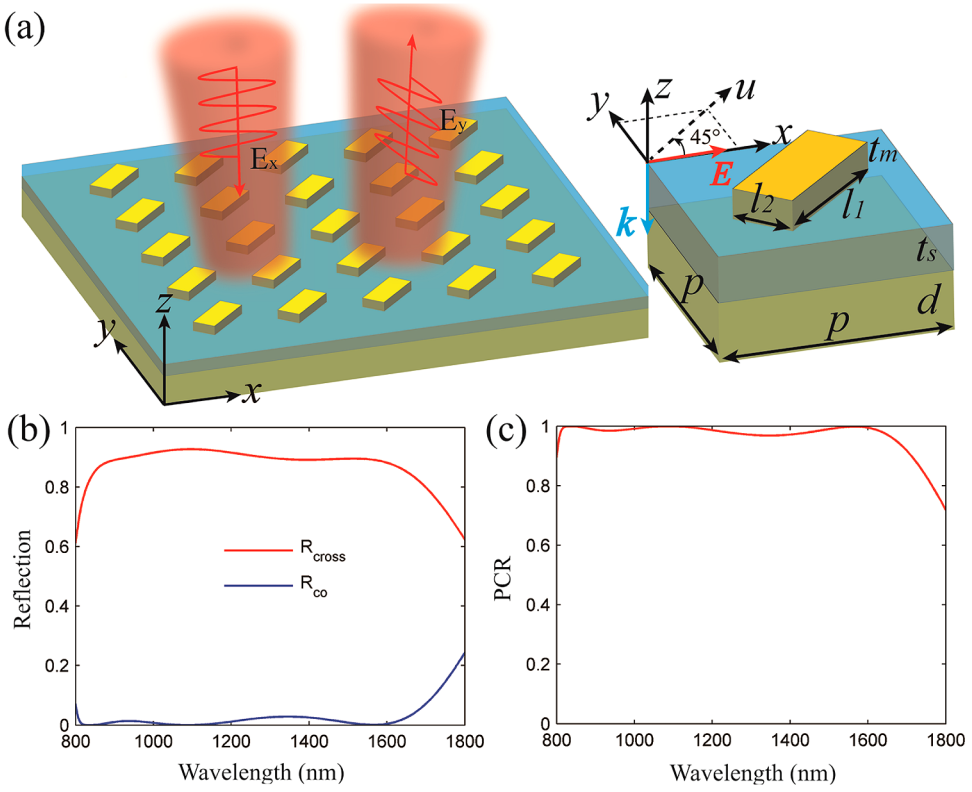

Figure 1. Geometry and working performance of our half-wave plate. (a) Schematic of the broadband plasmonic half-wave plate with dimensions $p = 600$ nm, $l_1 = 390$ nm, $l_2 = 165$ nm, $t_m = 80$ nm, $t_s = 110$ nm, and $d = 150$ nm. (b) Simulated reflection for the copolarized and cross-polarized light at normal incidence. (c) Simulated polarization conversion efficiency at normal incidence. The incident light is *x*-polarized.

propagation effect by introducing abrupt phase shifts with arrays of optical resonators, allowing spatial control over the phase of light, which can serve as ultrathin optical components for optical integration with significant advances over the current available technology.

Optical wave plates, one of the most important optical components, have attracted constant attention, where various metamaterials- or metasurfaces-based wave plates have been successfully investigated and demonstrated,[17−26] thus providing unprecedented opportunities to manipulate the polarization states of light along a subwavelength optical path. In spite of the success already achieved, there are still several issues that need to be solved. For example, in some of the designs with a single-resonator array, the phase retardation is realized by plasmonic resonance, resulting in a narrow operation band.[17−19] Detuning the plasmonic resonator away from their resonant wavelengths is a good approach to realize broadband polarization conversion.[20−24] Additionally, dispersion-free metastructures are used to broaden the operational bandwidth.[25,26] Another important issue is the extremely low polarization conversion efficiency of plasmonic metasurfaces, coming from the weak coupling between the incident and cross-polarized fields.[3,4] To increase the efficiency, it has been proposed to combine the electric (symmetric mode) and magnetic (asymmetric mode) plasmonic resonances. For instance, by combining a top metallic resonator array with a ground metal plane, a broadband terahertz half-wave plate with an efficiency of up to 80% between 0.8 and 1.36 THz has been successfully realized.[23] Furthermore, by replacing the metallic resonators with high-refractive-index silicon structures in combination with a silver ground plane, a dielectric meta-reflectarray-based half-wave plate with near-unity reflectance and over 98% polarization conversion efficiency has been experimentally demonstrated with a bandwidth of about 200 nm.[24] However, the bandwidth of the response is sharply reduced with increased incident angles, limiting the practical applications of the design.[24] Their performance[24] also comes at a price of a substantially thicker device in comparison to a typical plasmonic metasurface.

Here we demonstrate an ultrathin, broadband half-wave plate in the near-infrared range using a plasmonic metasurface. Our numerical simulations and optical characterization results show that the polarization conversion efficiency is over 95% with over 90% reflectance across an 800 nm bandwidth. Moreover, both simulated and experimental results indicate that this broadband and high-efficiency performance is supported over a wide range of incident angles. By integrating several plasmonic antennas with distinct geometries

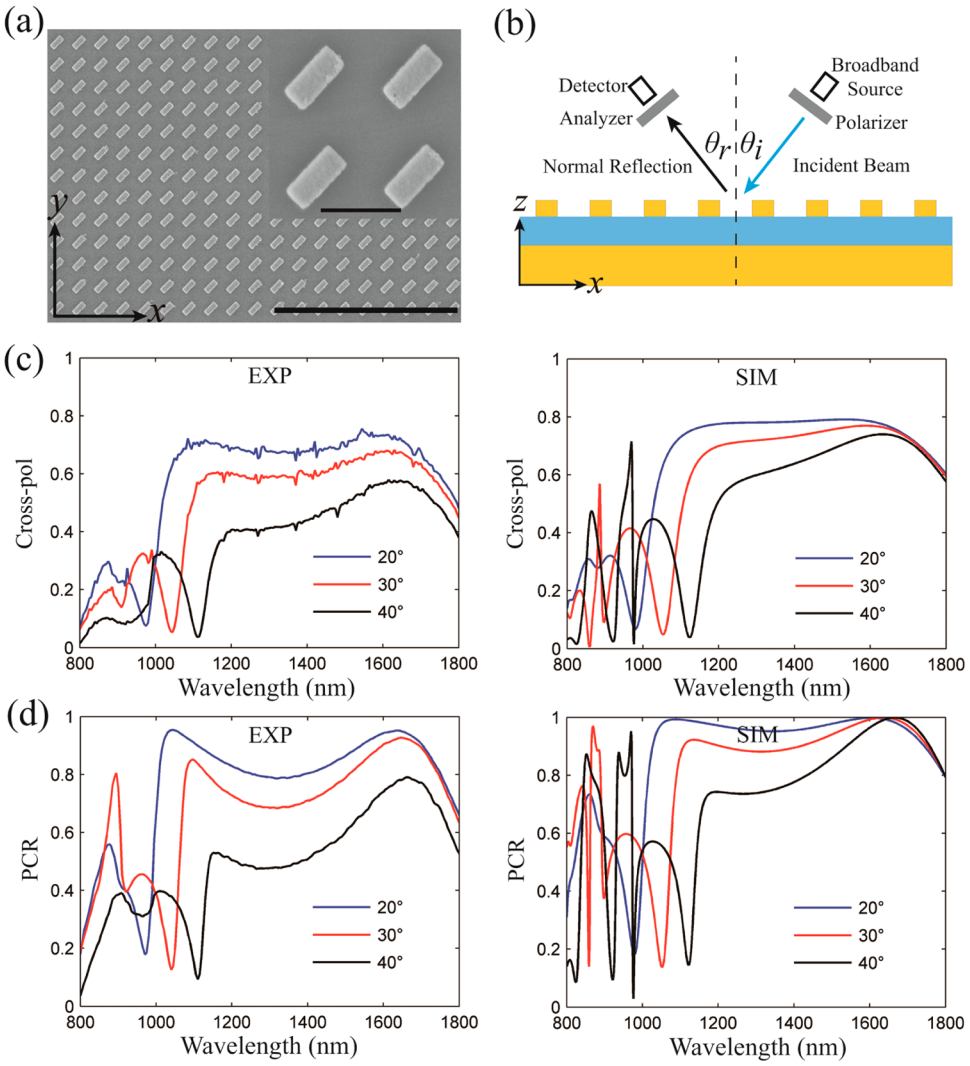

Figure 2. Optical characterization of the plasmonic half-wave plate. (a) SEM image of part of the fabricated sample (scale bar 5 μm). Local magnification is shown in the inset (scale bar 500 nm). (b) Experimental setup for the reflection measurement. (c) Measured (left panel) and simulated (right panel) normalized cross-polarized reflection for various incident angles. (d) Measured and simulated polarization conversion efficiency for various incident angles. The titanium (Ti) adhesion layers between the Au−SiO_2 interfaces are taken into consideration in the simulations. The incident light is *x*-polarized.

in a supercell, which can create a linear phase shift of the reflected cross-polarized light covering a 2π range, a broadband, high-efficient, and background-free half-wave plate has been experimentally realized as a periodic array of the integrated supercells.

RESULTS AND DISCUSSION

The schematic of the broadband half-wave plate is depicted in Figure 1a; the plate is composed of a periodic gold (Au) brick-shape nanoantenna array and a continuous Au film, separated by a silicon dioxide (SiO_2) dielectric layer. The topmost brick nanoantennas are aligned along their largest dimension (*u*-axis in Figure 1a), rotated counterclockwise by 45° with respect to the *x*-direction, and periodically distributed in both the *x*- and *y*-directions with a pitch of 600 nm. The other parameters of the brick nanoantenna are t_m = 80 nm, l_1 = 390 nm, l_2 = 165 nm. The thickness of the middle SiO_2 spacer layer is optimized (for the broadband and high-efficiency performance) to be 110 nm, and the bottom Au layer has a thickness of 150 nm. The optimal SiO_2 thickness is determined through a parameter sweep using simulations, and further discussion can be found in the Supporting Information, Section 1 and Figure S1.

The single-layer metasurfaces of V-shaped antennas allow for both transmission and reflection operation modes,[3,4] but their polarization conversion is somewhat limited. To improve the efficiency of polarization conversion, here we limit our design to operation in reflection mode by coupling the Au ground plane to the top brick resonators, therefore employing hybrid plasmonic modes.

We implement three-dimensional (3D) full-wave simulations using the finite element method (FEM) to verify the performance of the broadband half-wave

plate. In the simulation, the SiO_2 spacer is taken as a lossless dielectric with a constant refractive index of 1.45. The permittivity of Au in the near-infrared range is described by the Drude model with plasma frequency $\omega_p = 1.37 \times 10^{16}$ s^{-1} and damping frequency $\omega_d = 1.224 \times 10^{14}$ s^{-1}, which has taken the surface roughness and grain boundary effects into consideration.[27,28] Periodic boundary conditions are used in the *x*- and *y*-directions, and a plane wave is incident downward on the structure with the electric field polarized along the *x*-direction (or *y*-direction) as the excitation source. Figure 1b clearly indicates that the incident light is converted into its cross-polarized reflected light (R_{cr}), and the intensity of the copolarized reflection (R_{co}) is almost zero in the wavelength range from 800 to 1600 nm. The polarization conversion rate (PCR), defined as PCR = $R_{cr}/(R_{cr} + R_{co})$, is shown in Figure 1c, which remains above 95% from 805 to 1672 nm. The relative bandwidth of the half-wave plate, defined as WB = $2 \times (\lambda_l - \lambda_s)/(\lambda_l + \lambda_s)$, where λ_l and λ_s are the long and short limits of a wavelength range with PCR above 95%, respectively, reaches about 70%.

To experimentally validate the broadband linear polarization conversion, the plasmonic half-wave plate was fabricated using standard electron beam lithography (EBL) and a lift-off process. Figure 2a displays a scanning electron microscope (SEM) image of the fabricated sample. The overall lateral size of the sample is about 1 mm $\times$ 1 mm, which consists of 1667 $\times$ 1667 unit cells. Details of the fabrication process are given in the Methods section. The reflection spectra were measured using a variable-angle spectroscopic ellipsometer (J. A. Woollam Co., V-VASE) equipped with polarizers (see Methods). Figure 2b shows a schematic experimental setup for the reflection measurements. Due to the limitation of our ellipsometer setup, we were able to measure only the angle range with $\theta_i + \theta_r > 36°$ for which the receiver and emitter are well separated, with θ_i and θ_r being the incident and reflection angles, respectively.

The reflection and PCR are measured and calculated for three different incident angles θ_i and compared with the simulation results. Figure 2c and d confirm that the broadband and high-efficiency performance is sustained over a wide incident angle range, in contrast to the previously reported dielectric metal–reflectarray polarization converter, which appears to be very sensitive to the angle of incidence (when the incident angle is above 10°, the performance of polarization conversion is severely degraded).[24] The experimental data are in reasonable agreement with the simulated spectra considering the imperfection in the fabricating process. The discrepancy in the reflection amplitude may be ascribed to the imperfections and surface roughness of the topmost nanoantennas, resulting in additional scattering and absorption.

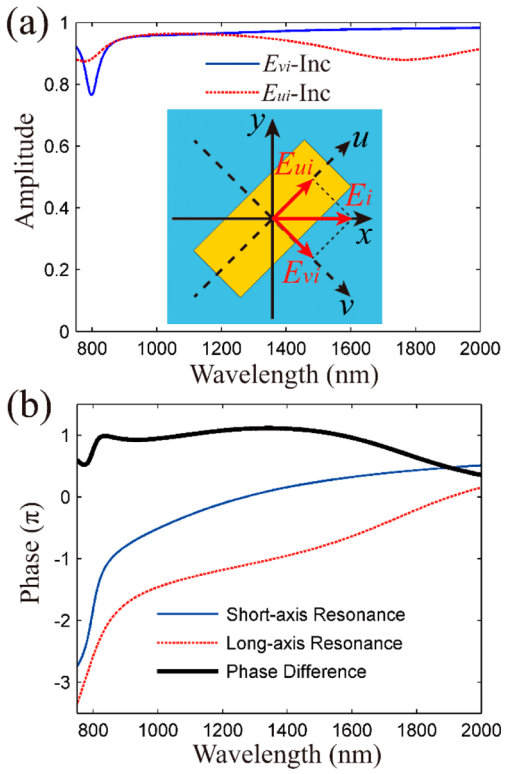

Figure 3. (a) Amplitude of the reflection coefficient ($|S_{11}|$) for the incident light polarized along the *u* (red dashed curve) and *v* (blue solid curve) axes. Inset shows that the *x*-polarized incident light (E_i) can be divided into two perpendicular components (E_{ui} and E_{vi}). (b) Reflection phase for the incident light polarized along the *u* (red dashed curve) and *v* (blue solid curve) axes and the corresponding relative phase difference (black solid curve).

At oblique incidence, several guided modes with high *Q*-factor at short wavelengths are excited, and the bandwidth of polarization conversion is reduced.

To understand the underlying mechanism of broadband linear polarization conversion, we take the *x*-polarized incident light (E_i) as an example and decompose it into two perpendicular components (E_{ui} and E_{vi}) to study the corresponding reflection response. The simulated amplitude and phase of the reflection are shown in Figure 3. When the incident electric field is linearly polarized only in the *x*-direction (or *y*-direction), the rotated nanoantenna supports the detuned orthogonal electric dipoles, which are excited by the electric field components along the *u*- and *v*-axis. The amplitudes of the reflection coefficient defining the detuned orthogonal electric dipoles are almost the same in the wavelength range where the half-wave plate works. At the same time, the relative phase difference nearly reaches π (black curve in Figure 3b), resulting in a 90° polarization rotation. The high polarization conversion efficiency here is ascribed to the superposition of the partial cross-polarized (copolarized) reflected fields within the Fabry–Perot-like cavity formed by the bottom Au plane and the topmost nanoantenna array, resulting in constructive

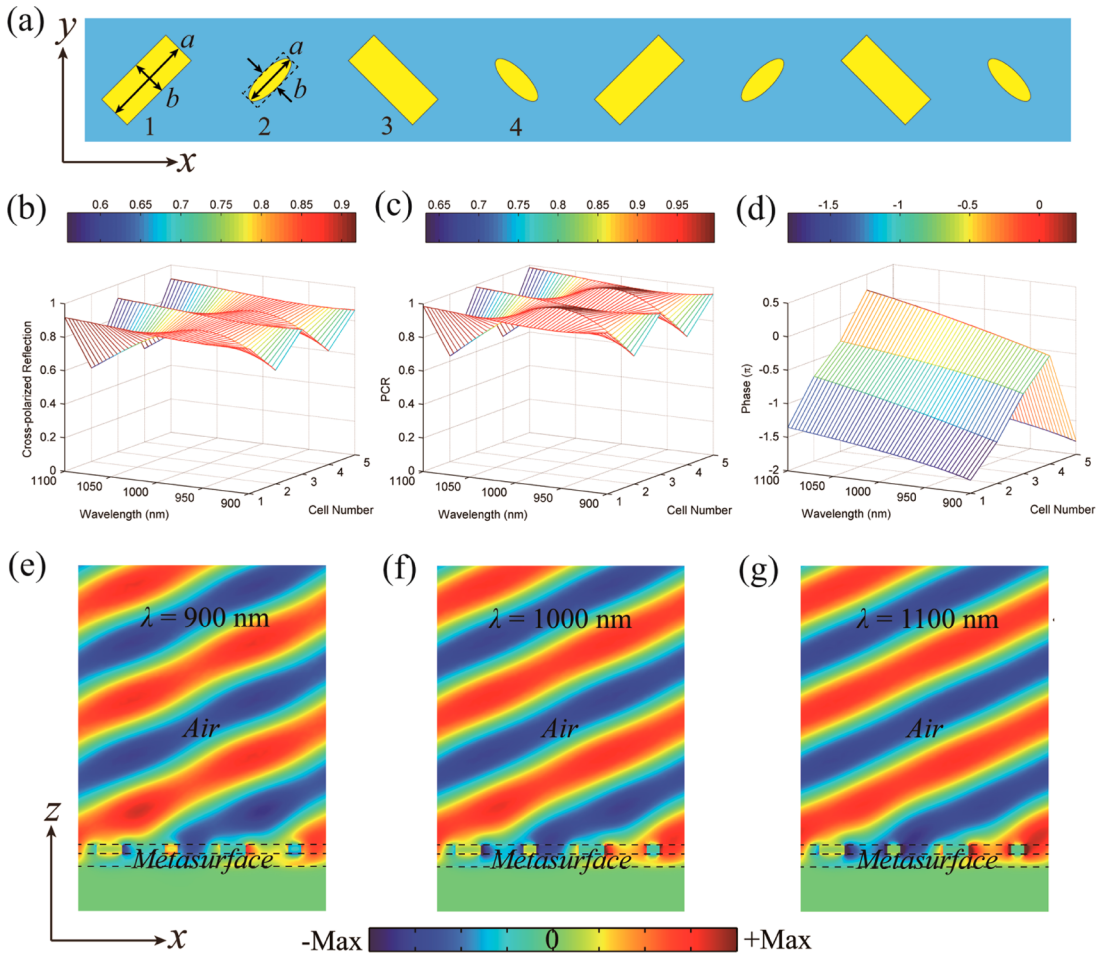

Figure 4. (a) Schematic of supercells containing four antennas that provide a phase shift from 0 to 2π. The dimensions of antenna 1 (nanobrick) are a = 440 nm and b = 175 nm, and the dimensions of antenna 2 (nanoellipse) are a = 275 nm and b = 95 nm. Antennas 3 and 4 are rotated by $\pi/2$ with respect to antennas 1 and 2, respectively. (b–d) Simulated cross-polarized reflection magnitude, polarization conversion rate, and cross-polarized reflection phase, respectively, for an array of four antennas as a function of incident wavelength. In all of the plots, antenna 5 is the same as antenna 1. (e–g) Cross-polarized electric field E_y distributions at 900, 1000, and 1100 nm, respectively. The x-polarized plane wave is normally incident on the metasurface.

(destructive) interference and nearly unity (zero) cross-polarized (copolarized) reflection.[23,24] Additionally, the working bandwidth of polarization conversion is approximately determined by the specific wavelengths of the long-axis and short-axis resonances (Supporting Information, Section 2 and Figure S2).[24]

The above designed half-wave plate can achieve high PCR over a wide wavelength spectrum. However, the copolarized reflected light cannot be eliminated completely. Then the converted cross-polarized light and the remaining copolarized reflected light will merge together in space. To separate the cross-polarized and copolarized reflected beams spatially and route the cross-polarized light in a designated direction, we have integrated several plasmonic antennas into a supercell to create a linear phase gradient of the cross-polarized reflected wavefront, resulting in anomalous reflection, guiding the cross-polarized light away. Each of those plasmonic antennas can serve as a half-wave plate with high efficiency, which is different from the V-shaped antenna-based metasurfaces,[3,4] where the anomalous (cross-polarized) reflected/refracted beams are weak, leading to inefficient light-manipulation effects. To validate this concept and simplify the design, four antennas are introduced by numerical simulations to form nearly a 2π phase shift coverage for the cross-polarized reflected light (Figure 4a). At a fixed wavelength of 1000 nm, each of these antennas achieve very similar cross-polarized reflection (above 85%) and a phase increment of about $\pi/2$ between adjacent cells; additionally, the designed metasurface works within a wide wavelength range. Figure 4b–d show the simulated cross-polarized reflection magnitude, PCR, and cross-polarized reflection phase, respectively, for these four antennas as a function of the incident wavelength between 900 and 1100 nm. It can be observed that the designed metasurface maintains high efficiency over a broad wavelength range of around 200 nm as the phase gradient for all four resonators remains approximately linear, thus enabling

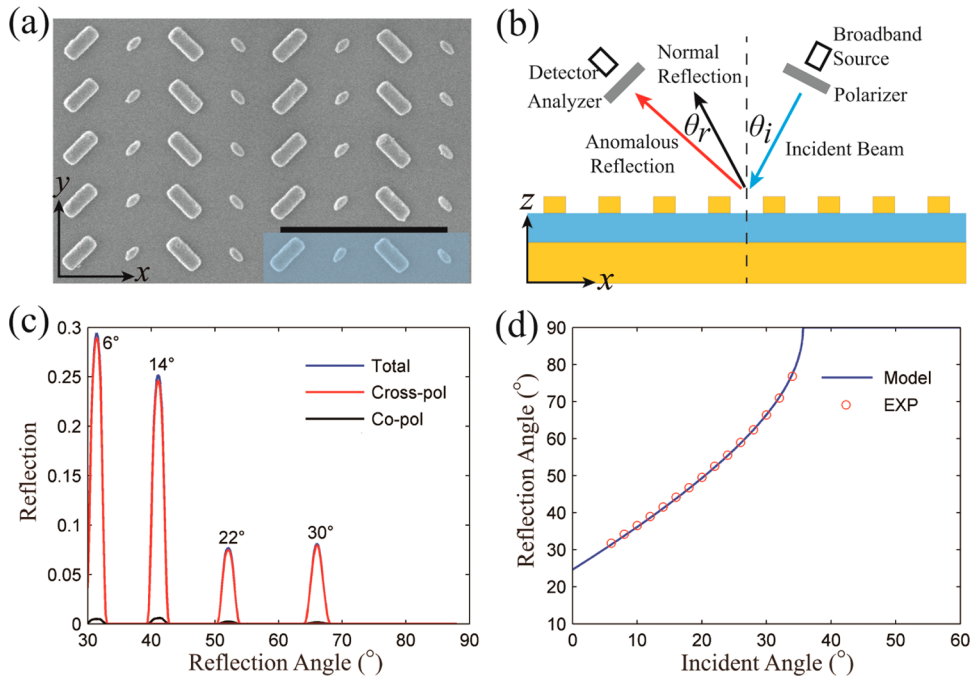

Figure 5. Characterizations of the metasurfaces containing supercells. (a) SEM image of part of one fabricated metasurface with a supercell highlighted by light blue color (scale bar 2 μm). (b) Schematic of the experimental setup for testing the metasurface. (c) Measured normalized reflection for the gradient metasurface under the illumination of *x*-polarized light at λ = 1000 nm with different incident angles. (d) Anomalous reflection angle θ_r as a function of the incident angle θ_i at λ = 1000 nm. The solid curve is the theoretical calculation from the generalized Snell's law, and the markers indicate the experimental data extracted from reflection measurements.

the broadband anomalous reflection for cross-polarized reflected light.

According to the generalized Snell's law,[3] this metasurface with a phase gradient should exhibit an anomalous reflection peak at an angle of $\theta_r = \sin^{-1}(\sin\theta_i + (\lambda/s))$ at an incident angle of θ_i, where $s = 2.4\ \mu$m is the period of the supercell along the *x*-direction. To verify the broadband anomalous reflection, the 3D full-wave numerical simulations were performed using the FEM. In the simulations, an *x*-polarized plane wave was normally incident on the metasurface supercell in an FEM domain with periodic boundary conditions set in both the *x*- and *y*-directions. The cross-polarized reflected electric fields E_y at several wavelengths (900, 1000, and 1100 nm) are plotted in Figure 4e–g, showing well-defined wavefronts. In addition, the reflected beams at λ = 1000 nm and λ = 1100 nm have less distortion, and the wavefronts closely resemble an ideal plane wave.

In order to validate the broadband anomalous reflection experimentally, the metasurface composed of supercells was fabricated, and the corresponding SEM image is shown in Figure 5a. The operation of the metasurface is tested as shown in Figure 5b. The incident ray is shown in blue, the normally reflected ray in black, and the anomalously reflected ray of interest in red. The sample was characterized with the same spectroscopic ellipsometer (see Methods). In our experiments, the receiver and emitter are separately mounted on two bases, which can freely rotate within a specific angle range, so that both θ_i and θ_r can be easily changed. Figure 5c shows the measured anomalous reflection intensity as a function of the reflection angle θ_r under various incident angles at the working wavelength of 1000 nm. As depicted in Figure 5c, we performed the measured result only when the incident angles are above 6°, as our experimental setup does not allow us to carry out the measurement within the angle region $\theta_i + \theta_r < 36°$, as otherwise the source and receiver would touch each other. For normally incident light, the calculated reflection angle is 22.02° for λ = 1000 nm, so the reflection signal cannot be detected. Fortunately, numerical simulations show that more than 84% of cross-polarized light under normal incidence would be reflected anomalously with an angle of about 22°, which is consistent with the result calculated from the generalized Snell's law. It can be seen that the cross-polarized reflection power (red curve in Figure 5c) coincides with the total reflection power (blue curve in Figure 5c), and the copolarized reflection power (black curve in Figure 5c) is almost zero, confirming the required performance. The ratio between the power of the desired and orthogonal polarizations is above 20 and the integrated PCR exceeds 95%. We can further quantitatively verify the generalized Snell's law by doing more measurements. Figure 5d depicts the anomalous reflection angle θ_r as a function of θ_i by identifying the peak positions in the measured reflection spectra at the wavelength λ = 1000 nm. Impressively, all the experimental data (red circles) are in excellent agreement with the

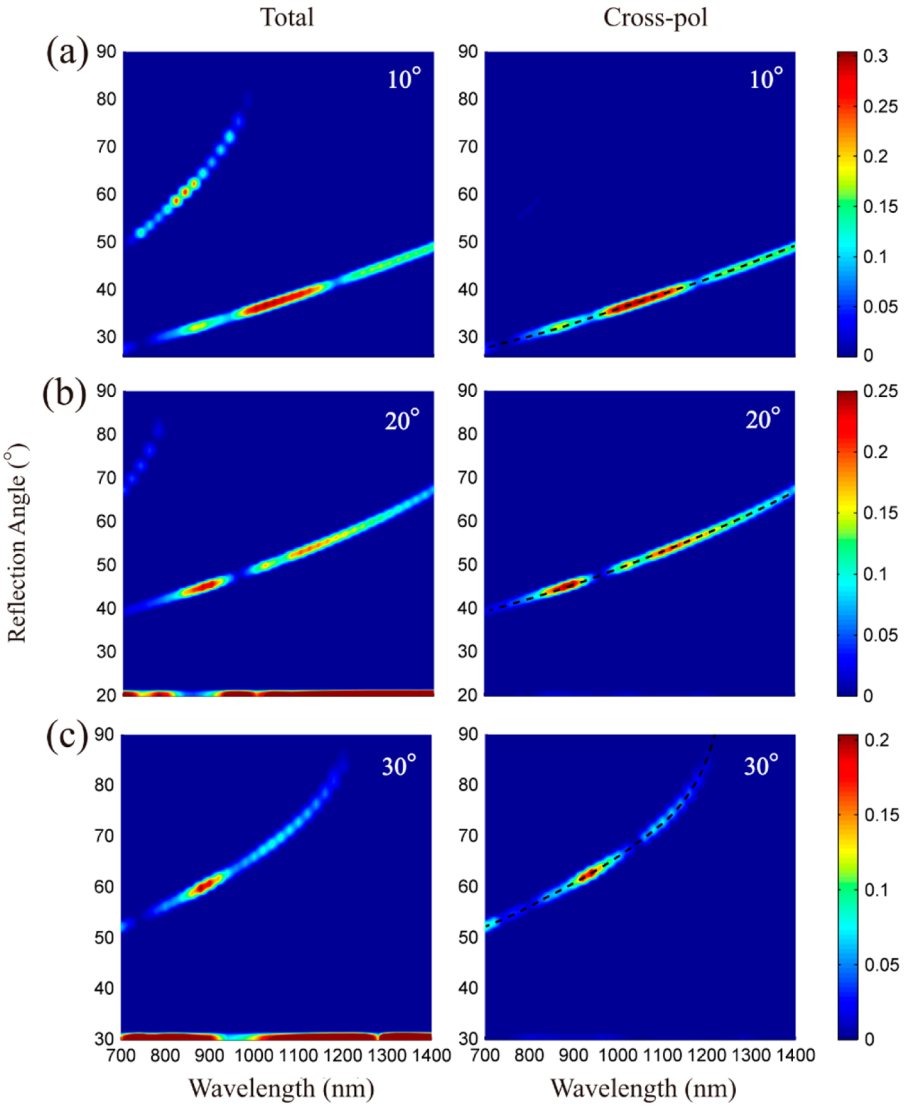

Figure 6. Broadband functionality of the metasurface. Experimentally measured normalized total reflection (left panels) and cross-polarized reflection (right panels) as a function of the wavelength λ and the reflected angle θ_r. The incident angles of the input beams are (a) 10°, (b) 20°, and (c) 30°, respectively. The dashed curves in the right panels are the theoretically calculated wavelength-dependent bending angles using the generalized Snell's law. The incident light is *x*-polarized.

theoretical result (blue solid curve), hence confirming that the generalized Snell's law applies.

Finally, we experimentally quantify the broadband functionality of the metasurface. The reflected field intensity for both polarizations was measured within a wavelength range from 700 to 1400 nm. In Figure 6a–c, we used two-dimensional color maps to show the total reflection (left panels) and cross-polarized reflection (right panels) as functions of incident wavelength and reflection angle, under illuminations with *x*-polarized input light at incident angles of 10°, 20°, and 30°, respectively. The experimental results clearly show that the cross-polarized beam is anomalously reflected to a wavelength-dependent reflection angle θ_r following the generalized law of reflection over a broad bandwidth. The theoretically calculated wavelength-dependent anomalous reflection angle is plotted as the dashed curve in the right panels of Figure 6, demonstrating excellent agreement with the experimental results. In our calculations, the reflection phase gradient is assumed to remain almost constant within the wavelength range of interest. Figure 6 also shows that the reflection angle θ_r increases with increasing wavelength at a fixed incident angle. In addition, the anomalous reflection intensity drops to zero for larger wavelengths (for example θ_i = 30°), where θ_r approaches 90° and the incident light will be converted into surface waves.[8] Yet another feature that remains unexplained is a copolarized reflected light at large reflection angles that appears in Figure 6a,b. These are the high-order diffraction modes attributed to the periodicity of the metasurface.[29]

CONCLUSIONS

In conclusion, we have demonstrated an ultrathin, broadband half-wave plate in the near-infrared range

using a plasmonic metasurface. Simulated results show that the polarization conversion efficiency is over 97% with over 90% reflectance across the 800 nm bandwidth. Moreover, simulated and experimental results demonstrate that this broadband and high-efficiency performance is sustained over a wide range of incident angles, up to 40°. Furthermore, by integrating several antennas with various geometries in a supercell, which can create a linear phase shift of the reflected cross-polarized light covering a 2π range, a broadband, highly efficient, background-free half-wave plate has been experimentally realized. This approach can be easily extended to any other relevant frequencies, such as the visible frequency, if the metal losses and fabrication challenges are taken into consideration. In addition, our results provide appropriate candidates for more advanced applications, for instance, broadband quarter-wave plate, planar imaging devices, and high-performance spatial light modulators.

METHODS

Fabrication of Plasmonic Metasurfaces. First, a 5 nm thick Ti adhesion layer is deposited onto a glass substrate, followed by evaporation of a 150 nm Au film, another 5 nm Ti adhesion layer, and a 110 nm SiO_2 film using electron beam deposition. Then, the sample was coated with a 220 nm thick e-beam resist PMMA (4% in anisole, Micro Chem) layer. Subsequently, the plasmonic metasurface was defined using e-beam lithography at the acceleration voltage of 100 keV. After exposure, the sample was developed in a solution of methyl isobutyl ketone (MIBK) and isopropyl alcohol (IPA) of MIBK:IPA = 1:3 for 50 s. Once the development of the resist was complete, a 5 nm Ti adhesion layer and a 80 nm gold layer were deposited sequentially using electron beam deposition. After a lift-off process performed using acetone, the Au patterns were finally formed on top of the SiO_2 film.

Optical Characterization. The reflection spectra were measured using the scatterometry mode of a spectroscopic ellipsometer (J. A. Woollam Co., V-VASE) equipped with polarizers. The light source is a xenon lamp with a broadband NIR spectrum. The diameter of the incident beam was set at 400 μm. The beam sequentially passed through a monochromator and a polarizer and then was incident on the sample. This broadband light source mounted on a base can be easily rotated to get various incident angles. The outgoing beam passed through an analyzer that filters the output at different polarizations and was collected by a detector. To test the performance of the metasurface composed of supercells, the detection is completed in scatterometry mode, which covers a broad range of scattering angles θ.

Conflict of Interest: The authors declare no competing financial interest.

Acknowledgment. This work was supported by U.S. Army Research Office grant 63133-PH (W911NF-13-1-0226) "Flat Photonics with Metasurfaces" and the Air Force Office of Scientific Research MURI grant "Active Metasurfaces for Advanced Wavefront Engineering and Waveguiding". F.D. would like to acknowledge the Chinese Scholarship Council (CSC, No. 201306320012) for financial support. F.D. and S.H. acknowledge the support by the National Natural Science Foundation of China (Nos. 91233208, 61271016, and 61178062) and the National High Technology Research and Development Program (863 Program) of China (No. 2012AA030402). Swedish VR grant no. 621-2011-4620 and AOARD are also acknowledged.

Supporting Information Available: The influence of the thickness of the middle SiO_2 spacer layer and the resonance modes of the broadband half-wave plate. This material is available free of charge *via* the Internet at http://pubs.acs.org.

REFERENCES AND NOTES

1. Kildishev, A. V.; Boltasseva, A.; Shalaev, V. M. Planar Photonics with Metasurfaces. *Science* **2013**, *339*, 1232009.
2. Yu, N.; Capasso, F. Flat Optics with Designer Metasurfaces. *Nat. Mater.* **2014**, *13*, 139–150.
3. Yu, N.; Genevet, P.; Kats, M. A.; Aieta, F.; Tetienne, J. P.; Capasso, F.; Gaburro, Z. Light Propagation with Phase Discontinuities: Generalized Laws of Reflection and Refraction. *Science* **2011**, *334*, 333–337.
4. Ni, X.; Emani, N. K.; Kildishev, A. V.; Boltasseva, A.; Shalaev, V. M. Broadband Light Bending with Plasmonic Nanoantennas. *Science* **2012**, *335*, 427–427.
5. Sun, S.; Yang, K.-Y.; Wang, C.-M.; Juan, T.-K.; Chen, W. T.; Liao, C. Y.; He, Q.; Xiao, S.; Kung, W.-T.; Guo, G.-Y.; *et al*. High-Efficiency Broadband Anomalous Reflection by Gradient Meta-surfaces. *Nano Lett.* **2012**, *12*, 6223–6229.
6. Pfeiffer, C.; Grbic, A. Metamaterial Huygens' Surfaces: Tailoring Wave Fronts with Reflectionless Sheets. *Phys. Rev. Lett.* **2013**, *110*, 197401.
7. Pors, A.; Albrektsen, O.; Radko, I. P.; Bozhevolnyi, S. I. Gap Plasmon-Based Metasurfaces for Total Control of Reflected Light. *Sci. Rep.* **2013**, *3*, 2155.
8. Sun, S.; He, Q.; Xiao, S.; Hu, Q.; Zhou, L. Gradient-Index Meta-Surfaces as A Bridge Linking Propagating Waves and Surface Waves. *Nat. Mater.* **2012**, *11*, 426–431.
9. Lin, J.; Mueller, J. B.; Wang, Q.; Yuan, G.; Antoniou, N.; Yuan, X. C.; Capasso, F. Polarization-Controlled Tunable Directional Coupling of Surface Plasmon Polaritons. *Science* **2013**, *340*, 331–334.
10. Huang, L.; Chen, X.; Bai, B.; Tan, Q.; Jin, G.; Zentgraf, T.; Zhang, S. Helicity Dependent Directional Surface Plasmon Polariton Excitation Using a Metasurface with Interfacial Phase Discontinuity. *Light: Sci. Appl.* **2013**, *2*, e70.
11. Aieta, F.; Genevet, P.; Kats, M. A.; Yu, N.; Blanchard, R.; Gaburro, Z.; Capasso, F. Aberration-Free Ultrathin Flat Lenses and Axicons at Telecom Wavelengths Based on Plasmonic Metasurfaces. *Nano Lett.* **2012**, *12*, 4932–4936.
12. Ni, X.; Ishii, S.; Kildishev, A. V.; Shalaev, V. M. Ultra-thin, Planar, Babinet-Inverted Plasmonic Metalenses. *Light: Sci. Appl.* **2013**, *2*, e72.
13. Pors, A.; Nielsen, M. G.; Eriksen, R. L.; Bozhevolnyi, S. I. Broadband Focusing Flat Mirrors Based on Plasmonic Gradient Metasurfaces. *Nano Lett.* **2013**, *13*, 829–834.
14. Ni, X.; Kildishev, A. V.; Shalaev, V. M. Metasurface Holograms for Visible Light. *Nat. Commun.* **2013**, *4*, 2807.
15. Huang, L.; Chen, X.; Mühlenbernd, H.; Zhang, H.; Chen, S.; Bai, B.; Tan, Q.; Jin, G.; Cheah, K.-W.; Qiu, C.-W.; *et al*. Three-Dimensional Optical Holography Using a Plasmonic Metasurface. *Nat. Commun.* **2013**, *4*, 2808.
16. Chen, W. T.; Yang, K. Y.; Wang, C. M.; Huang, Y. W.; Sun, G.; Chiang, I. D.; Liao, C. Y.; Hsu, W. L.; Lin, H. T.; Tsai, D. P. High-Efficiency Broadband Meta-Hologram with Polarization-Controlled Dual Images. *Nano Lett.* **2014**, *14*, 225–230.
17. Pors, A.; Nielsen, M. G.; Valle, G. D.; Willatzen, M.; Albrektsen, O.; Bozhevolnyi, S. I. Plasmonic Metamaterial Wave Retarders in Reflection by Orthogonally Oriented Detuned Electrical Dipoles. *Opt. Lett.* **2011**, *36*, 1626–1628.
18. Roberts, A.; Lin, L. Plasmonic Quarter-Wave Plate. *Opt. Lett.* **2012**, *37*, 1820–1822.
19. Yang, B.; Ye, W.-M.; Yuan, X.-D.; Zhu, Z.-H.; Zeng, C. Design of Ultrathin Plasmonic Quarter-Wave Plate Based on Period Coupling. *Opt. Lett.* **2013**, *38*, 679–681.

20. Pors, A.; Nielsen, M. G.; Bozhevolnyi, S. I. Broadband Plasmonic Half-Wave Plates in Reflection. *Opt. Lett.* **2013**, *38*, 513–515.
21. Zhao, Y.; Alù, A. Tailoring the Dispersion of Plasmonic Nanorods to Realize Broadband Optical Meta-Waveplates. *Nano Lett.* **2013**, *13*, 1086–1091.
22. Cong, L.; Xu, N.; Gu, J.; Singh, R.; Han, J.; Zhang, W. Highly Flexible Broadband Terahertz Metamaterial Quarter-Wave Plate. *Laser Photonics Rev.* **2014**, *8*, 626–632.
23. Grady, N. K.; Heyes, J. E.; Chowdhury, D. R.; Zeng, Y.; Reiten, M. T.; Azad, A. K.; Taylor, A. J.; Dalvit, D. A.; Chen, H. T. Terahertz Metamaterials for Linear Polarization Conversion and Anomalous Refraction. *Science* **2013**, *340*, 1304–1307.
24. Yang, Y.; Wang, W.; Moitra, P.; Kravchenko, I. I.; Briggs, D. P.; Valentine, J. Dielectric Meta-Reflectarray for Broadband Linear Polarization Conversion and Optical Vortex Generation. *Nano Lett.* **2014**, *14*, 1394–1399.
25. Jiang, S.-C.; Xiong, X.; Hu, Y.-S.; Hu, Y.-H.; Ma, G.-B.; Peng, R.-W.; Sun, C.; Wang, M. Controlling the Polarization State of Light with a Dispersion-Free Metastructure. *Phys. Rev. X* **2014**, *4*, 021026.
26. Shaltout, A.; Liu, J.; Shalaev, V. M.; Kildishev, A. V. Optically Active Metasurface with Non-Chiral Plasmonic Nanoantennas. *Nano Lett.* **2014**, *14*, 4426–4431.
27. Liu, N.; Mesch, M.; Weiss, T.; Hentschel, M.; Giessen, H. Infrared Perfect Absorber and Its Application as Plasmonic Sensor. *Nano Lett.* **2010**, *10*, 2342–2348.
28. Yuan, H. K.; Chettiar, U. K.; Cai, W. S.; Kildishev, A. V.; Boltasseva, A.; Drachev, V. P.; Shalaev, V. M. A Negative Permeability Material at Red Light. *Opt. Express* **2007**, *15*, 1076–1083.
29. Larouche, S.; Smith, D. R. Reconciliation of Generalized Refraction with Diffraction Theory. *Opt. Lett.* **2012**, *37*, 2391–2393.